Carbon 161 (2020) 169–180

Contents lists available at ScienceDirect

Carbon

journal homepage: www.elsevier.com/locate/carbon

Effect of molybdenum particles on thermal and mechanical properties of graphite flake/copper composites

Qianyue Cui [a, 1], Cunguang Chen [a, 1], Chengwei Yu [a], Tianxing Lu [a], Haiming Long [a], Shuhao Yan [a], Alex A. Volinsky [b], Junjie Hao [a, *]

[a] Institute for Advanced Materials and Technology, University of Science and Technology Beijing, 100083, Beijing, China
[b] Department of Mechanical Engineering, University of South Florida, Tampa, 33620, USA

ARTICLE INFO

Article history:
Received 15 August 2019
Received in revised form
10 January 2020
Accepted 18 January 2020
Available online 23 January 2020

ABSTRACT

Graphite flakes (GFs) in the GF/Cu composites generally fail to exert the advantage of the negative coefficient of thermal expansion (CTE) on account of the weak interfacial bonding between GFs and Cu. In this work, a rivet-joint strategy is adopted to surmount the dilemma. By introducing submicron Mo particles into the Cu matrix through the chemical synthesis process, various GF/Cu composites with the improved alignment of GFs via the method of tape-casting and hot-pressing sintering have been prepared. Due to the combined effects of Mo particle strengthened Cu and the rivet-joint interfacial architecture deriving from the in-situ synthesized Mo_xC, optimized thermal/mechanical properties of GF/Cu–Mo composites have been achieved. The 50 *vol%* GF/Cu composite with 1 *wt%* Mo shows the in-plane thermal conductivity of 598 $W \cdot m^{-1} \cdot K^{-1}$ and the through-plane CTE of -2.92×10^{-6} K^{-1} (25–100 °C). Simultaneously, the bending strength is 40% higher than the 50 *vol%* GF/Cu composite. This strategy could promote the development of composites with improved combined structural and functional properties.

1. Introduction

Further increase of the dissipated power in microelectronic components has become the bottleneck for the next generation of integrated circuits (ICs) and three-dimensional (3D) electronics [1]. As a high-efficiency channel for heat transfer, thermal management materials with high thermal conductivity (TC) and suitable coefficient of thermal expansion (CTE) can extend dense electronic system life and keep its efficiency.

In the actual application, significant differentiation in heat transfer requirements has driven the development of new types of well-performing thermal management materials [2]. Metal matrix composites (MMCs) acquire customizable thermal and mechanical properties by adjusting the suitable ratio of matrix and reinforcement material in order to better meet the specific needs of the heat-removal systems [3–8]. Copper has one of the highest TC (400 $W \cdot m^{-1} \cdot K^{-1}$), except for silver, as along with excellent toughness, workability and corrosion resistance. Different allotropes of carbon have a unique place in heat sinks in terms of their splendid thermal properties, such as diamond (1000–2300 $W \cdot m^{-1} \cdot K^{-1}$), graphene (> 3000 $W \cdot m^{-1} \cdot K^{-1}$), carbon nanotubes (3000–3500 $W \cdot m^{-1} \cdot K^{-1}$), graphite (100–2000 $W \cdot m^{-1} \cdot K^{-1}$), etc. [9–12].

Two-dimensional (2D) graphite flakes (GFs) have the in-plane TC of 500–1900 $W \cdot m^{-1} \cdot K^{-1}$ and the through-plane TC of 10–20 $W \cdot m^{-1} \cdot K^{-1}$. Owing to the unique anisotropic thermal and stable physicochemical properties, graphite-reinforced copper matrix composites are under intensive investigation because of their superior TC and adjustable CTE can meet the special applications in the thermal management field. The GFs intrinsic anisotropy makes the alignment of the reinforcement materials in the matrix, a key factor that affects composite properties [13–16]. Chu et al. [17] prepared Cu/graphene composites by depositing the Cu/graphene suspension, in which graphene was well-dispersed and highly aligned. The in-plane TC of Cu/graphene composite reached record-high 525 $W \cdot m^{-1} \cdot K^{-1}$ with the graphene volume fraction of 35%, benefiting from the construction of a long-range and highly aligned graphene network in the copper matrix.

The chemical inertness between copper and carbon, causes the poor interfacial adhesion of carbon-reinforced copper composites, resulting in undesirable thermal and mechanical properties of Cu/C

* Corresponding author.
E-mail address: haojunjie@ustb.edu.cn (J. Hao).
[1] These authors contributed equally to this work.

https://doi.org/10.1016/j.carbon.2020.01.059
0008-6223/

composites [18–21]. Therefore, it is well accepted that the optimized Cu–C interface is a way to promote comprehensive properties of the Cu/C composite. Modified carbon materials have been frequently used for improving the wettability between metal and carbon materials [22–28]. The carbon reinforcements were directly plated on the metal or carbide films, which could combine metal matrix with the carbon reinforcements in the composite preparation process. Furthermore, the addition of strong carbide forming elements, such as Cr, B, Ti, was also utilized for changing chemical constituent of the metal matrix [26,29–32], which could reduce the surface tension of the melt copper and interfacial tension in the process for wetting the carbon materials. The surface modification of carbon materials as well as the matrix alloying affect the properties of metal/C composites through amending the interphase of the composites. It is noteworthy that low interfacial thermal contact resistance between copper and graphite during the high-temperature and high pressure preparation is attributed to the slide of graphite and deformation of softened copper [22,23].

Nevertheless, "uncleaned" Cu–C interface, caused by carbides (ZrC, TiC, B_4C, SiC, etc.) or other phases (Mo, Ti, Si, Cr, C, etc.), leads to aggravating phonon scattering at the interface, so that the TC of composite decreases. Even so, the enhancement of the Cu–C interface contributes to higher bending strength and lower CTE of the composite [18,33,34]. Li et al. [29] utilized titanium to modify the interface between copper and diamond. The results showed that the heterogeneous nucleation of titanium carbide appeared at the Cu-diamond interface at high temperature and TiC layers thickened with increasing Ti content. The TC of diamond/Cu-χTi composites first increased and then decreased. It was perceived that the appropriate thickness of TiC layers intensified phonon transfer across the interface. Otherwise, an excessively thick TiC layer was harmful to heat transfer from copper to diamond on account of its low intrinsic TC of 21 $W \cdot m^{-1} \cdot K^{-1}$. Bai et al. [22] concentrated on the effects of B_4C coating layers on the thermal/mechanical properties of the graphite flake/Cu (GF/Cu) composite. The B_4C coating contributed to strong chemical bonding between graphite and copper, which increased the bending strength from 94 *MPa* to 142 *MPa*. However, the B_4C layers also increased the phonon scattering at the Cu-graphite interface, and slightly brought down the TC of composite. Chen et al. [35] studied the effects of the nickel coatings on the GFs on the thermal expansion behaviors of the GF/Cu composites. The Cu-GF interfacial bonding had been significantly enhanced owing to the introduction of Ni–P plating layer on GFs, contributing to the better thermal properties. The Z-CTE of 50GF/Cu composite sharply dropped from $10 \times 10^{-6}\ K^{-1}$ to $-2 \times 10^{-6}\ K^{-1}$. However, the XY-CTE changed slightly with different thickness of nickel coatings on the GFs.

The optimization of the interfacial composition and morphology of the interfacial phase is an available approach for improving thermal and mechanical performance of MMCs.

In this study, 50 vol% GF/Cu (50GF/Cu) composites with Mo addition were prepared via tape-casting and hot-pressing sintering. The tape-casting process was used to ensure the highly ordered arrangement of the graphite flakes. The matrix alloying method with the strong carbide forming element, Mo, was employed to improve the interface bond strength between the copper and the graphite reinforcement. Furthermore, in order to simultaneously achieve mechanical strength and ductility of the composites, Mo as the strengthening particles should be of the micro-nano size. Herein, the ammonium molybdate tetrahydrate (AMT) was introduced into the copper matrix as the Mo precursor, and ultrafine Mo particles were obtained after the decomposition and reduction of AMT. The microstructure and the thermal/mechanical properties of the composites with different mass fraction of Mo are systematically discussed.

2. Experimental methods

2.1. Raw materials

Electrolytic copper powder (99.9%, D_{50} = 10 μm, General Research Institute for Nonferrous Metals, China) was used as metal matrix. The graphite flakes (D_{50} = 270 μm, thickness = 50 μm, Alfa Aesar Chemical Co., Ltd) were used as the thermal enhancement material. Ammonium molybdate tetrahydrate (analytical reagent, Shanghai Aladdin Bio-Chem Technology Co. Ltd, China) was used as the Mo precursor. Ethanol (analytical reagent), polyvinyl butyral (PVB, analytical reagent), and dibutyl phthalate (DBP, analytical reagent) were the components of the organic system for tape-casting.

2.2. Preparation of bulk GF/Cu composites

The samples were prepared by tape-casting and hot-pressing sintering, and the preparation process of the GF/Cu–Mo composites is shown in Fig. 1. The first step was mix the raw material powders. Cu powders were mixed with AMT powders in varying proportions by ball-milling for 12 *h*. The diameter of milling balls was 15 *mm* and 8 *mm*, and the quality ratio was M_{15}:M_8 = 2:1. Ball-to-powder weight ratio was 1:3. Subsequently, 50 *vol%* of GFs with mixed Cu/AMT powders were added into the mixer without balls to prevent GFs from fracture and blended for 3 *h*. A few drops of petrol were also added into the premixed copper powders and GFs, which could hinder the copper powder sedimentation under the influence of gravity after mixing.

The second step was the preparation of the green tape. The slurry for tape casting was a complex multicomponent organic system containing powders, solvent, binder, and plasticizer. The organic system must have low vaporization temperature, be chemically stable and not react with copper powders and GFs. The ethanol solution (boiling point of 78.4 °C) with 7 *wt%* PVB was used as binder to guarantee the green tape strength, and 1 *wt%* DBP was added as plasticizer to ensure the green tape toughness. The mass ratio of the pre-mixed powder to the binder is 1:1. The well-stirred slurry was directly cast into thin films onto a platform with a doctor. The GF/Cu green tape film was natural dried for 12 *h* at room temperature. The obtained film was flexible and could be readily cut into small slices. The debinding process of the green tape was then carried out in air at 400 °C for 2 *h*, and the deoxidation process was carried out in hydrogen at 850 °C for 2 *h*.

The last step was hot-pressing sintering. The stacks of multilayer slices were enclosed into a graphite mould. The GF/Cu composite was prepared by hot-pressing sintering in the argon atmosphere at 1000 °C for 2 *h*, under 10 *MPa* axial pressure.

2.3. Characterization

The microstructure and interfacial structure of the GF/Cu–Mo composites were observed by field emission scanning electron microscope (FE-SEM, HITACHISU 8010, Japan). The element distribution was analyzed by Energy Dispersion Spectra (EDS) attached to the FE-SEM. X-ray photoelectron spectroscopy (XPS, Kratos AXIS ULTRA^{DLD}, Japan) was employed to analyze the valence state of Mo in the composites. Transmission electron microscope (TEM, FEI F20, USA) was used to characterize the interfacial configuration and constitution of the composites. X-ray diffraction (XRD, RIGAKUTTR3, Japan) was used to analyze the phase composition of the composites. The thermal diffusivity coefficient (α) of the composites was measured in two directions (XY and Z) at room temperature by the laser flash method (NETZSCH LFA447, Germany) with the sample size of 10 × 10 × 3 mm. We defined the directions

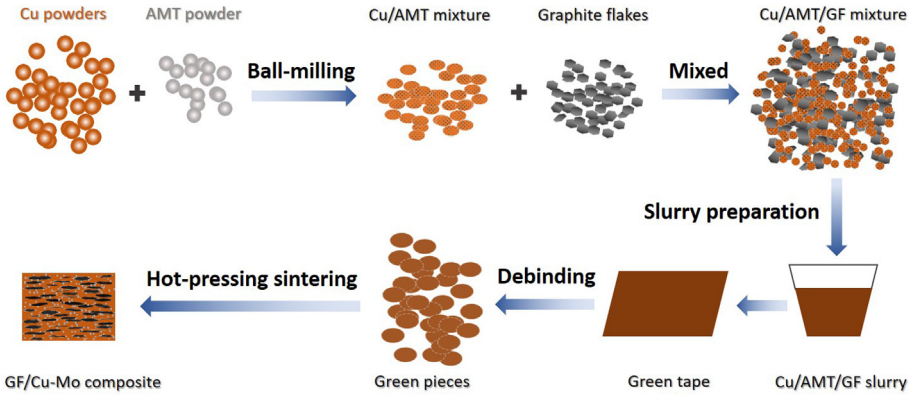

Fig. 1. Schematic illustration of the GF/Cu–Mo composites. (A colour version of this figure can be viewed online.)

paralleled and perpendicular to the GF basal plane as XY and Z directions, respectively. The density (ρ) of the composites was measured by the Archimedes' principle. The value of the composite specific heat capacity (C_p) was the sum of the specific heat capacity multiplied by the mass fraction of each component. The TC of the composites could be calculated by multiplying the thermal diffusivity coefficient, density and specific heat capacity. Three-point bending tests were carried out to measure the bending strength of the composites in two directions. The CTE of the composites was measured in the 25–250 ˚C range by the thermal dilatometer (NETZSCH DIL 402 PC, Germany).

3. Results and discussion

3.1. Microscopic morphology and phase composition

Fig. 2(a) shows typical microstructure of the 50GF/Cu composite. It can be observed that there were no obvious pores in the compact Cu matrix. GFs were arranged in a highly ordered manner. The pieces of GFs were approximately parallel to each other. Fig. 2(b) shows the microstructure of the Cu-GF interface, and the well-bonded Cu-GF interface without apparent cracks or pores, attributed to the hot-pressing sintering and pressure cooling process.

The sintering temperature, sintering pressure and soaking time were found to remarkably affect the density of the sample. Cu powders softened at high temperature and deformed under pressure in the hot-pressing sintering process. It was noted that the compact GF/Cu composites were difficult to be prepared at 1000 ˚C and the Cu matrix would be squeezed out above 1000 ˚C. Thus, 1000 ˚C was chosen as the appropriate sintering temperature. Besides, the sintering pressure of 10 *MPa* and soaking time of 2 *h* were the optimized parameters to obtain dense GF/Cu composites with 99% of theoretical density. Mo particles were added to the GF/Cu composites in a small amount, resulting in no obvious characteristic peaks in XRD analysis. Furthermore, XPS and TEM were adopted to explore the phase structure of Mo in the composites. The XPS survey spectra of the 50GF/Cu–1Mo composite in the 200 *eV* to 600 *eV* range is shown in Fig. 3(a), which revealed the presence of Cu, C, and Mo elements in the composite. The deconvolution of the Mo3d signal is shown in Fig. 3(c). The characteristic peaks of Mo3d at 228.3 *eV*, 231.5 *eV*, 232.5 *eV* and 235.6 *eV* are assigned to $Mo^{2+}3d_{5/2}$, $Mo^{2+}3d_{3/2}$, $Mo^{6+}3d_{5/2}$, $Mo^{6+}3d_{3/2}$, consistenting with the XPS data for the molybdenum carbide and molybdenum oxide phases [24,25,36]. Fig. 3(b) depicted the characteristic peaks of C1s at 284.4 *eV*, 284.8 *eV*, 285.5 *eV* and 288.4 *eV*, consistenting with the XPS data for the functional groups of carbide and carbon phase (Mo_2C, C – C, C = O and O – C = O, respectively.) [37].

The TEM analysis of the 50GF/Cu–1Mo composite (in Fig. 4) revealed the existence of the molybdenum carbide phase at the Cu-GF interface. The EDS analysis was carried out to investigated points A, B and C. It was found that most of Mo was at the interlayer between Cu and GF. The interlayer phase connected Cu and GF tightly with no microporosity or microcracks. The electron diffraction pattern in Fig. 4b verified the existence of the simple substances of copper, graphite, molybdenum and the molybdenum carbide phase. Combined with the XPS data analysis, it could be inferred that the Mo particles at the Cu-GF interface closely contacted with GFs and reacted with the GFs at high temperature and pressure. The formation of molybdenum carbide filled some microcracks between Cu and GFs. Most Mo particles were still embedded in Cu matrix. This suggested that Mo existed in the composite. Given that Cu did not react with Mo or GF, the existence of Mo_2C should demonstrate the reaction between Mo and GF at high temperature.

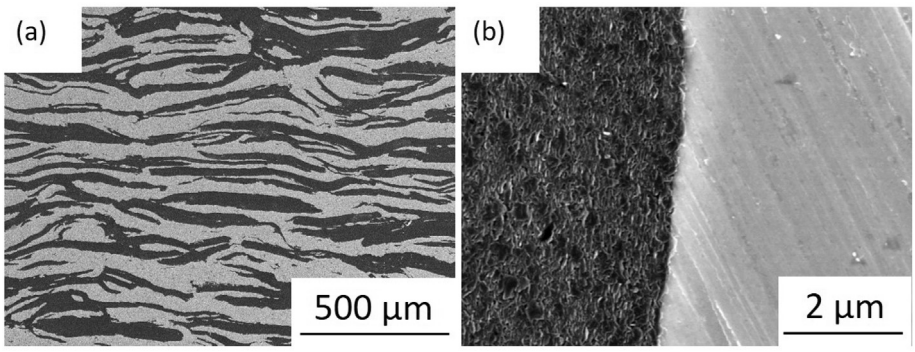

Fig. 2. Typical SEM images of: (a) 50GF/Cu composites and (b) Cu-GF interface.

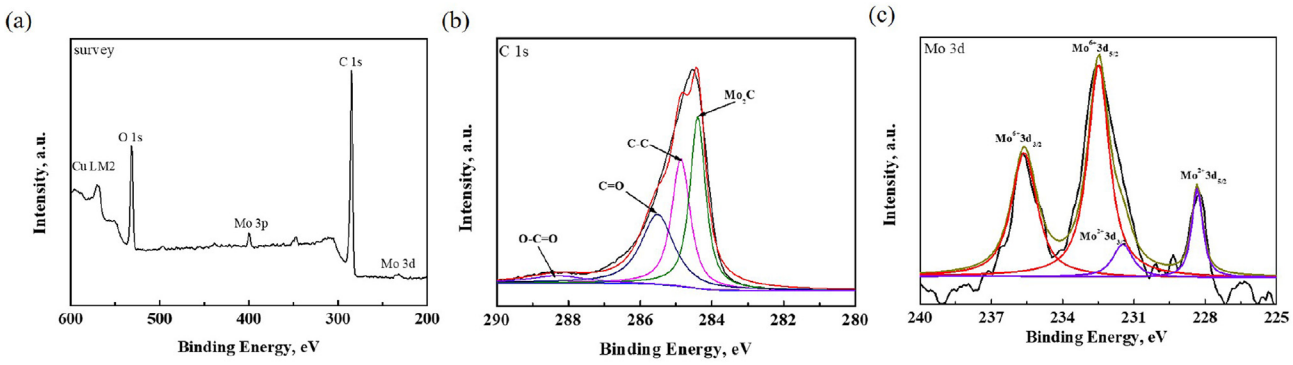

Fig. 3. (a) XPS survey spectra; (b) C1s spectra and (c) Mo3d spectra of Mo_2C in the Cu−1Mo/Cu composite. (A colour version of this figure can be viewed online.)

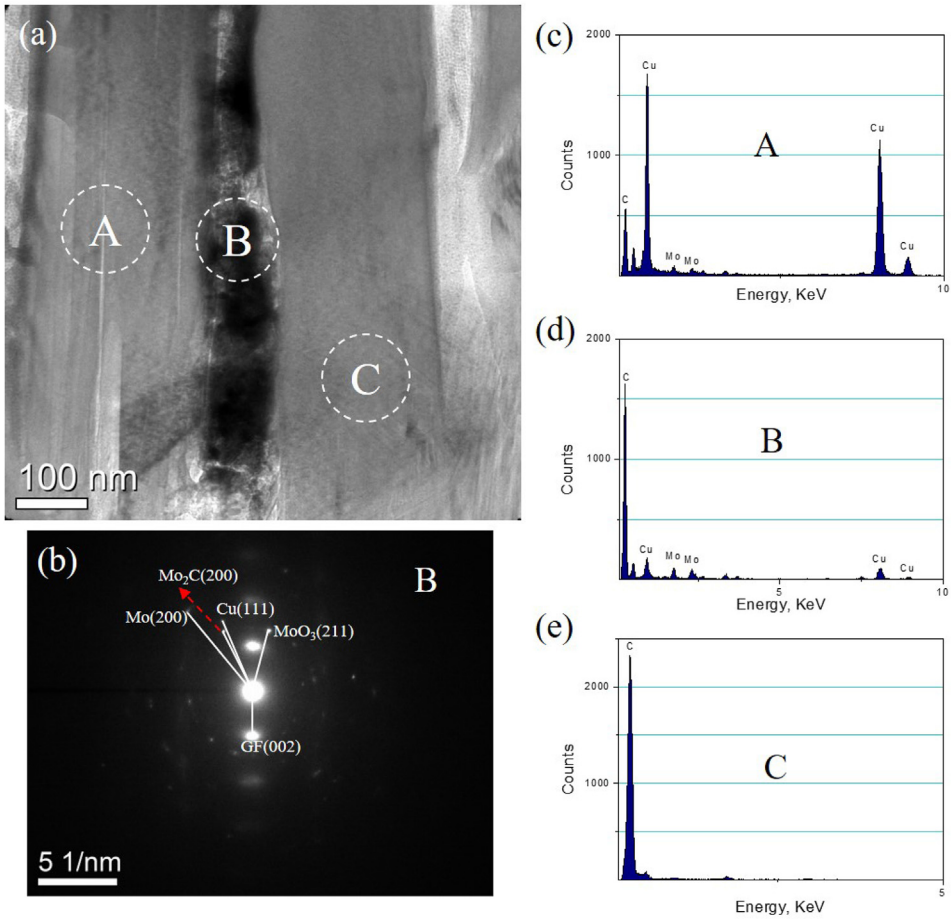

Fig. 4. (a) TEM image of the 50GF/Cu−1Mo composite interface; (b) the electron diffraction pattern and analysis of the marked point B in (a); (c), (d) and (e) EDS data of the marked points A, B and C in (a), respectively. (A colour version of this figure can be viewed online.)

3.2. Microstructure of the Cu matrix and the interface

In this study, given that the preparation of ultrafine Mo powders obtained from AMT obey the rules shown in Fig. 5, the main reactions can be described by Eq. (1-3). It has been reported that a ternary gaseous molybdenum compound $MoO_2(OH)_2$ was generated in the hydrogen reduction process of MoO_3 owing to the presence of water vapor, which was responsible for the chemical vapor transports (CVT) mechanism, very similar to the hydrogen reduction preparation of W powder [38]. Initially, Mo phase was synthesized directly by reaction 1 and nucleated on the unreacted MoO_3. Then, the ternary gaseous molybdenum compound was formed via reaction 2, which could significantly accelerate the transport of Mo through the gas phase (reaction 3) and lead to the formation of Mo with a large particle size.

$$MoO_3 + 3H_2 = Mo + 3H_2O \quad (1)$$

$$MoO_3 + H_2O = MoO_2(OH)_2 \quad (2)$$

$$MoO_2(OH)_2 + H_2 = Mo + 4H_2O \quad (3)$$

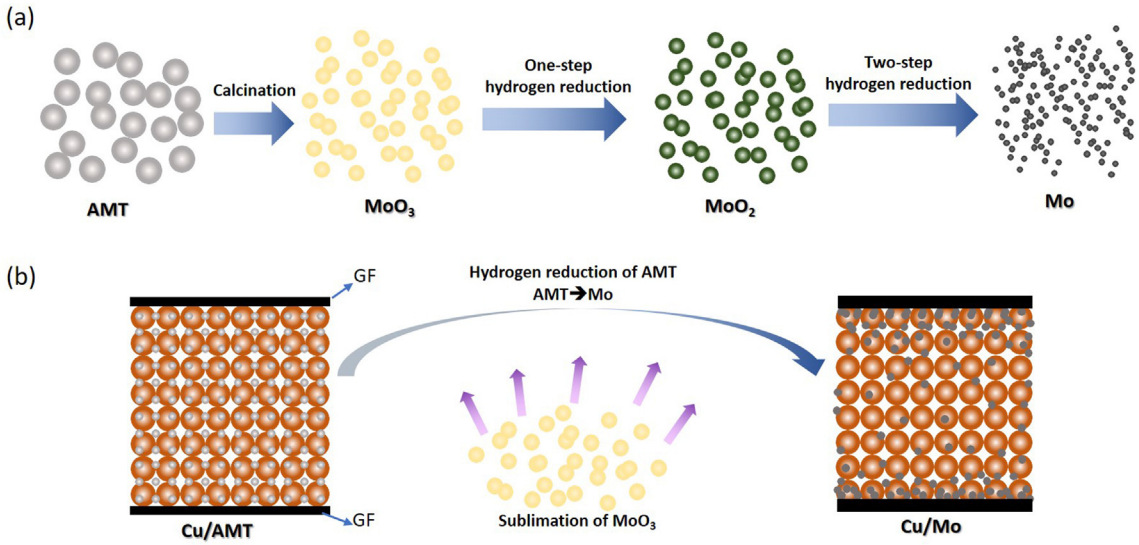

Fig. 5. Schematic illustration of (a) preparation of Mo powders and (b) the transport process of Mo in the Cu matrix. (A colour version of this figure can be viewed online.)

During the reduction process of the composite powder, MoO_3 in the Cu matrix turned into gaseous particulates, escaping from the Cu powders. Fortunately, GFs mixed in the Cu powders formed barriers to deposit the gaseous particulates in the composites. MoO_3 was finally reduced to submicron Mo powders. Fig. 6(a–i) display the SEM images of the 50GF/Cu–Mo composites and the Cu–Mo alloys without GFs after acid etch, and Table 1 list the corresponding EDS results of Mo contents in Fig. 6(a-g, i). It was

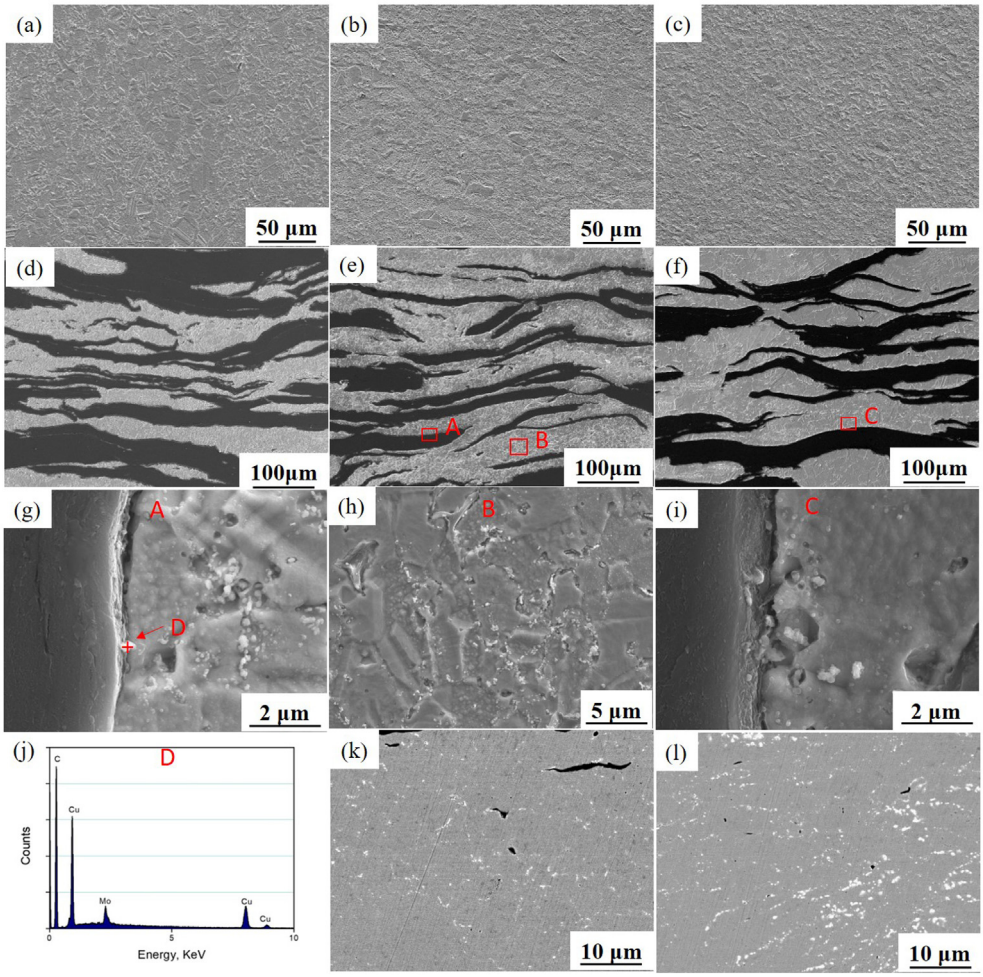

Fig. 6. SEM images of (a–c) Cu–Mo alloys and (d–f) 50GF/Cu–Mo composites after acid etch; (g–i) the enlarged view of area A, B and C in (e) and (f); (j) EDS spectra of point D in (g); (k, l) backscattered images of 50GF/Cu–1Mo and 50GF/Cu–3Mo composites. (a, d: 0.5 *wt*% Mo; b, e, g, h, k: 1 *wt*% Mo; e, f, i, l: 3 *wt*% Mo). (A colour version of this figure can be viewed online.)

Table 1
EDS results of the Cu–Mo alloys and the 50GF/Cu–Mo composites, as shown in Fig. 6

Areas	(a)	(b)	(c)	(d)	(e)	(f)	(g)	(i)
Mo content, wt%	0.37	0.51	2.26	0.51	0.97	2.82	0.73	0.79

found that the same AMT addition resulted in different Mo content in the GF/Cu–Mo composites and Cu–Mo alloys. Mo content of the former was higher than the latter, indicating that the GFs were the main constructions to the gaseous particles. The distribution of Mo particles was also another key factor that could affect the properties of GF/Cu composites. Fig. 6(g) and (i) show that the Mo particles with the average size of 200–500 nm are scattered at the interface of the GF/Cu–Mo composites. The Mo content of the GF/Cu–1Mo composite and the GF/Cu–3Mo composite at the Cu-GF interface was 0.73 *wt%* and 0.79 *wt%*, respectively. The EDS results suggested that a large number of Mo particles were dispersed in the matrix instead of segregated near GFs, and there were more Mo particles in the matrix of the GF/Cu–3Mo composite than in the GF/Cu–1Mo composite. Besides, the Mo particles presented in the matrix were found to be mainly distributed at Cu grain boundaries, as shown in Fig. 6(h). Backscattered SEM images show the distribution of Mo in the matrix of the GF/Cu–Mo composite in Fig. 6(k, l). It was observed that deposited Mo clusters appeared in the Cu matrix of the GF/Cu–3Mo composite, and no obvious Mo clusters in the GF/Cu–1Mo composite. The greater Mo concentration would accelerate the nucleation and growth of the ternary gaseous molybdenum compound particles in the Cu matrix. As a result, excess Mo particles tended to aggregate together in the matrix of the GF/Cu–3Mo composite.

To clearly investigate the grains characteristics of the GF/Cu–Mo composites, the EBSD results are shown in Fig. 7. The black areas above the images are uncalibrated graphite phase. It can be observed that Cu grains without submicron Mo particles were much larger than in the GF/Cu–Mo composites. Interestingly, the Cu grain size grew with increased Mo content, attributed to the agglomeration of Mo particles, as shown in Fig. 6(k, l). Simultaneously, it was found that the size of the Cu grains was both large and small. The distribution of Mo particles in the Cu matrix and the change of the Cu grain size could demonstrate that the in-situ submicron Mo particles contributed to the refinement of the Cu matrix grain. Because of no solid solubility of Mo in Cu matrix, the in-situ Mo particles acted as the reinforcements to block the dislocation motion and grain boundary movement so that the grain growth was inhibited. However, it was important to control the size and distribution of Mo particles for a better strengthening effect.

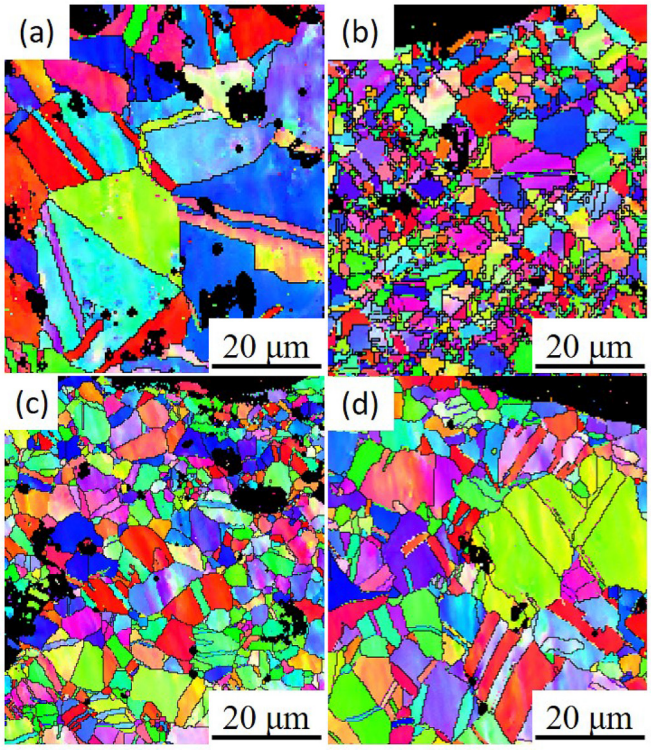

Fig. 7. EBSD patterns of 50GF/Cu composites with: (a) 0 *wt%* Mo, (b) 0.5 *wt%* Mo, (c) 1 *wt%* Mo and (d) 3 *wt%* Mo. (A colour version of this figure can be viewed online.)

Combining the analysis of the Mo formation mechanism, the grain size of the GF/Cu–Mo composites showed variation seen from Fig. 7. The size of grains without Mo reached up to 20 *μm*. When 0.5 *wt%* Mo was introduced into Cu matrix, the grains were refined sharply with the size of 1–5 *μm*. However, there were still 10 *μm* individual grains in Fig. 7(b), presenting nonuniform grain size distribution on account of the uneven Mo formation. As for the 1 *wt%* Mo addition in Fig. 7(c), the grains were 5 *μm*. Nonetheless, with increasing Mo content to 3 *wt%*, the composite grains grew up significantly, as seen in Fig. 7(d). This could be explained by the aggregation of Mo particles in the Cu matrix so that the effect of grain refinement was obviously weakened in some areas.

Additionally, it was found that some novel Mo particles existed in the Cu-GF interface, connecting Cu and GFs like a "rivet" in Fig. 8. The schematic diagram of the action mechanism of the Mo "rivet" is displayed in Fig. 8(g), and the generated Mo_2C particles closely contacted with GFs were like the "rivet head". By virtue of the high-temperature diffusion and reaction between Mo and C, the Mo "rivet" strongly bonded the surface layer of GFs with Cu matrix. The rivet-joint structure should be a good solution for improving the interface bonding between the two materials with poor wettability, for instance, Cu and graphite. The relevant bonding performance will be discussed below.

3.3. Thermal properties

3.3.1. Thermal conductivity and modeling

Table 2 depicts the thermal conductivity of 50GF/Cu composites in the different directions with various Mo content. On the one hand, the XY-TC of the composite with 50 *vol%*GF was 69.6% higher than pure copper (400 $W \cdot m^{-1} \cdot K^{-1}$), whereas the Z-TC of the 50GF/Cu composite was only about 15% of pure copper, which exhibited obvious anisotropy due to high alignment of the GFs. On the other hand, the introduction of Mo apparently decreased the TC of the composite. With the increasing mass fraction of Mo, the XY-TC of the composite steadily reduced, and the Z-TC decreased slightly. It was well accepted that the Kapitza resistance and thermal contact resistance were two key factors that affected thermal properties of MMCs [14,39]. The thermal contact resistance caused by the interface crack was greatly improved under the preparation conditions of high temperature and high pressure. However, the in-situ formed Mo and Mo_2C reduced the TC of the GF/Cu–Mo composite because of the increasing Kapitza resistance, which is attributed to the increasing phonon scattering at the Cu-GF interface [22–24]. This is also one explanation of the continuous reduction of the composite TC with the increasing Mo content.

It was observed that the XY-TC of the composite decreased by 9.85% with 0.5 *wt%* Mo addition, and decreased by 14.05% with 3 *wt%* Mo addition. This suggested that the influence mechanism of Mo content on the TC of the GF/Cu composites was diversified and

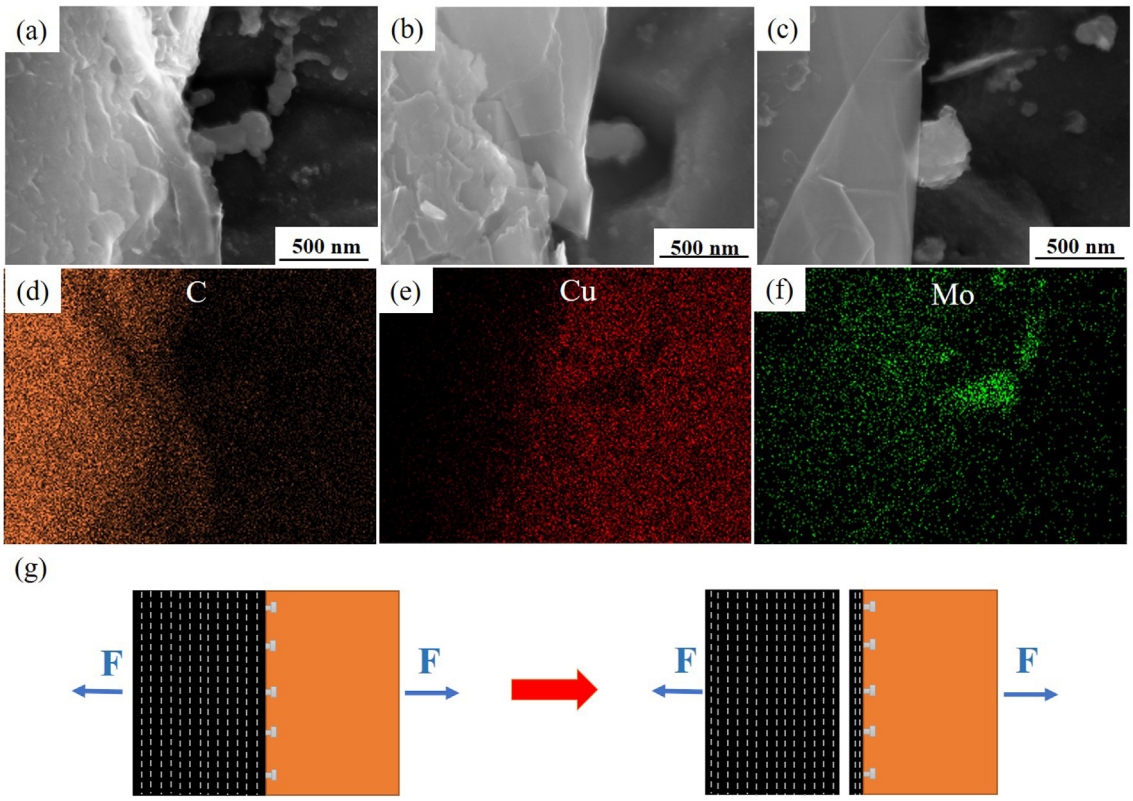

Fig. 8. Mo particles at the Cu-GF interface of 50GF/Cu composites with: (a) 0.5 *wt*% Mo, (b) 1 *wt*% Mo and (c) 3 *wt*% Mo, respectively. EDS patterns of (d) C, (e) Cu and (f) Mo in (a). (g) The schematic diagram of the action mechanism of the Mo "rivet" at the Cu-GF interface. (A colour version of this figure can be viewed online.)

non-equalized. Particularly, the Mo content affected the Z-TC of the composite under the same rule. Mo particles were found to disperse in the grains of the copper matrix in the 50GF/Cu–Mo composite in Fig. 6. Nevertheless, it was found that Mo particles at the Cu-GF interface did not increase as expected with higher Mo content. The increasing Mo content mostly existed in the Cu matrix, which reduced the matrix TC. This suggested that the introduction of Mo affected heat transfer behavior of the GF/Cu composites mainly by pinning the Cu-GF interface.

Moreover, the alignment of the anisotropic reinforcements, such as GFs, was another important factor in promoting thermal properties of composites. To verify the availability of tape casting in enhancing the orientation of GFs in the GF/Cu composite, the effective medium approximation (EMA) model was used to predict the values of the composite TC [39,40]. Taking into account all factors containing the intrinsic TC of Cu and GFs, size and orientation of GFs, the Kapitza resistance, the EMA model can be expressed as follows:

$$K_C = K_{Cu}\frac{2+f\left[\beta_1(1-L_1)\left(1+<cos^2\theta>\right)+\beta_3(1-L_3)\left(1-<cos^2\theta>\right)\right]}{2-f\left[\beta_1 L_1\left(1+<cos^2\theta>\right)+\beta_3 L_3\left(1-<cos^2\theta>\right)\right]} \tag{4}$$

Table 2
Thermal conductivity of 50GF/Cu composites with different Mo content.

Mo content, *wt*%	ρ, $g\cdot cm^{-3}$	α, $mm^2\cdot s^{-1}$		TC, $W\cdot m^{-1}\cdot K^{-1}$	
		XY	Z	XY	Z
0	5.5±0.1	274.5±1.5	23.2±0.5	678.6±3.7	57.3±1.2
0.5	5.4±0.1	250.5±1.0	19.5±0.2	613.2±2.4	47.8±0.5
1	5.4±0.1	244.3±1.2	18.9±0.4	598.0±2.9	43.4±1.0
3	5.4±0.1	238.2±1.0	17.7±0.2	582.2±2.4	42.3±0.5

with

$$\beta_i = \frac{K_{GF}^{eff} - K_{Cu}}{K_{Cu} + L_i\left(K_{GF}^{eff} - K_{Cu}\right)} \tag{5}$$

$$<cos^2\theta> = \frac{\int \rho(\theta) cos^2\theta sin\theta d\theta}{\int \rho(\theta) sin\theta d\theta} \tag{6}$$

Here, K_{Cu} is the TC of Cu, θ is the angle between the basal plane of the GFs and the defined XY-plane, $\rho(\theta)$ is a distribution function of GF orientation, and f is the volume fraction of the GFs. L_i is related to the GFs diameter (270 μm) and thickness (20 μm), and $L_1 = 0.0532$, $L_3 = 0.8936$. β_i were obtained by derivation of Eq. (5). K^{eff} is the effective TC of materials, which can be expressed as follows:

$$K^{eff} = \frac{K_0}{\frac{2K_0}{hD}+1} \tag{7}$$

Here, D and K_0 represent the inclusion particles size and intrinsic TC, and h ($=10^9$ $W\cdot m^{-1}\cdot K^{-1}$) is the interfacial thermal conductivity between the matrix and the inclusion. We ignored Kapitza resistance and took the intrinsic TC of GF as the effective TC because of the huge interfacial thermal conductivity between Cu and C. Therefore, $K_{Cu} = 400$ $W\cdot m^{-1}\cdot K^{-1}$, $K_{GF}^{XY} = 1000$ $W\cdot m^{-1}\cdot K^{-1}$ were adopted [41]. Then, Eq. (4) can be simplified as follows:

$$K_{xy} \cong 400 \times \frac{2+f\left(1.07+2.01\times\langle cos^2\theta\rangle\right)}{2-f\left(-3.85+4.02\times<cos^2\theta>\right)} \tag{8}$$

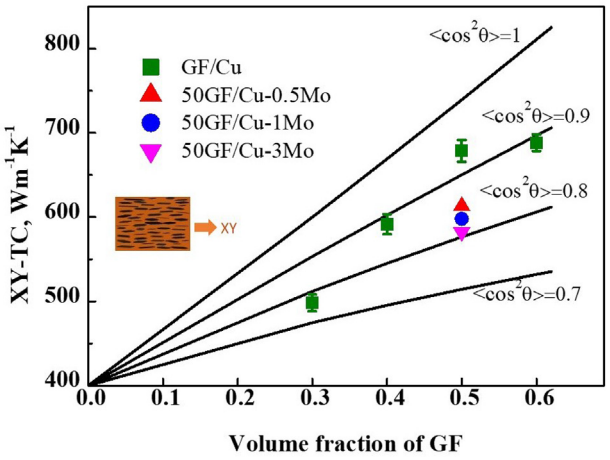

Fig. 9. TC of GF/Cu composites in the XY direction with different GF and Mo content as well as the theoretical predictions of GF/Cu by effective medium approximation (EMA) model with different distribution function of GF orientation ($< cos^2 >$). (A colour version of this figure can be viewed online.)

Fig. 9 showed the comparison of the measured and predicted values, with $< cos^2\theta > = 0.7, 0.8, 0.9, 1$. Based on the assumption of the non-Kapitza resistance, the XY-TC of 30GF/Cu composite without Mo addition was close to the predicted value with $< cos^2\theta > = 0.8$. Meanwhile, the measured value of XY-TC was closer to the predicted value with $< cos^2\theta > = 1$ and increasing volume fraction of GFs. Moreover, the 50GF/Cu XY-TC almost coincided with the predicted value with $< cos^2\theta > = 0.94$, which was higher than the distribution function of GF or graphene orientation in other studies [17]. It can be indicated that GFs dispersed in the Cu matrix with high alignment and high volume fraction of GFs contributed to their order.

In general, tape casting was an effective method for enhancing GFs alignment. Dramatically, the introduction of Mo reduced the heat conduction of the GF/Cu composites because of the "unclean" interfaces.

3.3.2. Thermal expansion properties

Fig. 10 described the change of the relative length and CTE of the 50GF/Cu–Mo composites with temperature ranged from 25 °C to 250 °C. Through the comparison of measured value and various models, including the rule of mixture (ROM) ($8 \times 10^{-6}K^{-1}$), the Kerner ($6.95 \times 10^{-6}K^{-1}$) [42] and the Turner ($2.94 \times 10^{-6}K^{-1}$) models [43], it was noted that the former was much higher than the latter. Ren et al. [30] verified that the effective contact area played an important role in affecting the CTE of the composite. The effective contact area between Cu and GFs was less than 10% of the total surface area because of high alignment of the GFs, which limited the inhibitory effect of GFs on the expansion of Cu matrix [44]. It was already known that the microcracks around the embedded GFs were modified at high temperature under pressure in the sintering process. However, owing to the lack of strong pinning between Cu and GF, the Cu-GF interface slid during raising temperature (no pressure during CTE measurement), which invalidated the advantage of GFs low CTE. The introduction of Mo obviously reduced the XY-CTE of the composite, indicating that the in-situ Mo and Mo_2C effectively optimized the Cu-GF interface. Nevertheless, the results also showed that the XY-CTE of the 50GF/Cu–Mo composites were slightly content dependent, which may be attributed to the weak Van Der Waals forces between GF interlayers. It is verified that the sliding fracture of GFs easily occurred under stress because of the weak Van Der Waals forces between GF interlayers [45].

It is noteworthy that the Z-CTE of the composite reached $9 \times 10^{-6}K^{-1}$, pertaining to the same magnitude with the CTE of semiconductor materials ($3–8 \times 10^{-6}K^{-1}$). The Z-CTE of the 50GF/Cu composite was much lower than Cu ($17 \times 10^{-6}K^{-1}$) or through-plane of GF ($28 \times 10^{-6}K^{-1}$). To explain this counterintuitive behavior, Firkowska et al. [14] considered Cu/GF composites as sandwich-like structure objects, and deduced the correlation between the equivalent through-plane CTE of the GF and other parameters based on the elasticity theory. The calculated results of equivalent CTE of GF and Cu were $-26 \times 10^{-6}K^{-1}$ and $24 \times 10^{-6}K^{-1}$, respectively. Besides, Ren et al. [30] thought that the

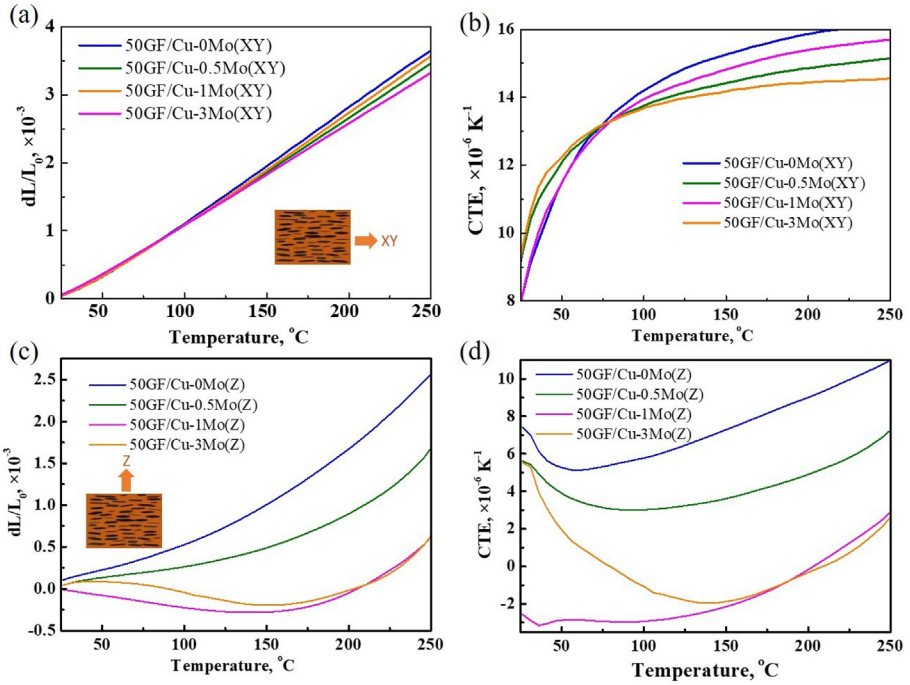

Fig. 10. The variation trend of the relative length and CTE (XY and Z directions) of the 50GF/Cu–Mo composites in the temperature range of 25–250 °C. (A colour version of this figure can be viewed online.)

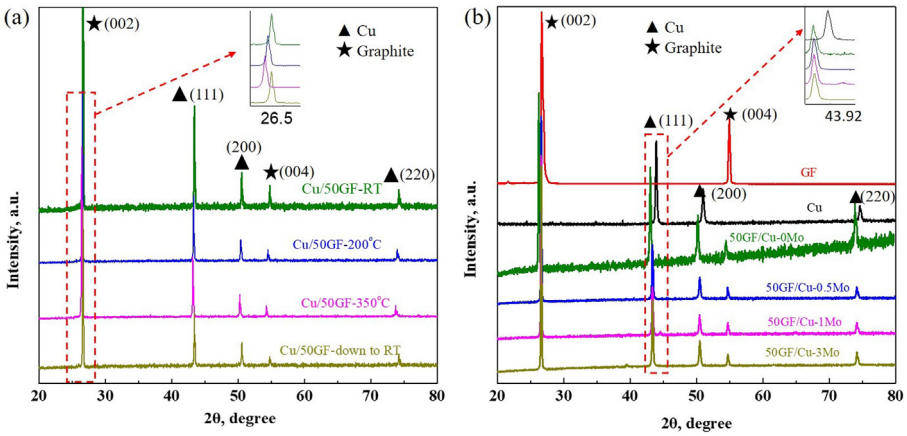

Fig. 11. XRD spectrum of (a) 50GF/Cu composite at different temperature points and (b) 50GF/Cu–Mo composites with different Mo content. (Both in the Z direction). (A colour version of this figure can be viewed online.)

introduction of alloying elements would lift the thermal stress in the composites, which further decreased the equivalent through-plane CTE of the GF and caused lower Z-CTE of the GF/Cu composite. Similarly, the aggregated Mo particles at the Cu-GF interface, and Mo "rivet" in the GF surface acted as a Mo "net". The Mo "net" sharpened the change of the through-plane elastic constants of the Cu and GF, aggravating the thermal expansion anomaly phenomenon (negative thermal expansion) in the Z direction. Interestingly, the Z-CTE of the GF/Cu–3Mo composite was higher than the GF/Cu–1Mo composite. This abnormal phenomenon could be explained by the unanticipated distribution of Mo particles in the GF/Cu composites with increasing Mo content. The Mo content in the composites is listed in Table 1, showing the intensified agglomeration of Mo particles in the Cu matrix. Mo clusters in the GF/Cu–3Mo composite (Fig. 6) caused lower CTE value of the Cu matrix compared with the GF/Cu–1Mo composite, narrowing the difference of the CTE values between the Cu matrix and the in-plane direction of GFs. Therefore, it could be inferred that the thermal stress between Cu and GF in the GF/Cu–3Mo composite was lower than in the GF/Cu–1Mo composite, which caused the equivalent through-plane CTE of the GF in the GF/Cu–3Mo composite to be higher than in the GF/Cu–1Mo composite. As a result, the Z-CTE of the GF/Cu–3Mo composite was higher than in the GF/Cu–1Mo composite.

To thoroughly explore the thermal expansion behavior of the 50GF/Cu–Mo composites, the XRD spectra at room and high temperatures were analyzed. Fig. 11(a) shows the XRD spectra of the 50GF/Cu composite at room temperature (RT), 200 °C, 350 °C and C-RT (from 350 °C cooled to RT). It could be observed that the peaks of Cu and GF at 200 °C and 350 °C shifted towards left by about 0.12° and 0.24°, respectively, compared to the peaks at RT. The shift results signified that the lattice constant of the Cu and GFs increased, which demonstrated the thermal expansion behavior of the Cu particles and GF interlayers when heated. Interestingly, comparing the XRD spectra of the 50GF/Cu-χMo (χ = 0.5, 1, 3) composites and the raw materials at RT (Fig. 11(b)), it was found that the Cu characteristic peaks of the as-prepared 50GF/Cu composite shifted left by about 0.5 °, but the GF peaks shifted slightly, which indicated that the residual thermal stress mostly existed in the Cu matrix, and the Cu particles were acted upon by the residual tensile stress. In the CTE test process of the composites, on the one hand, the internal residual thermal stress of the composites released slowly with temperature, which eased the lattice deformation (larger lattice constant). On the other hand, higher temperature enlarged the lattice constant of Cu particles and the

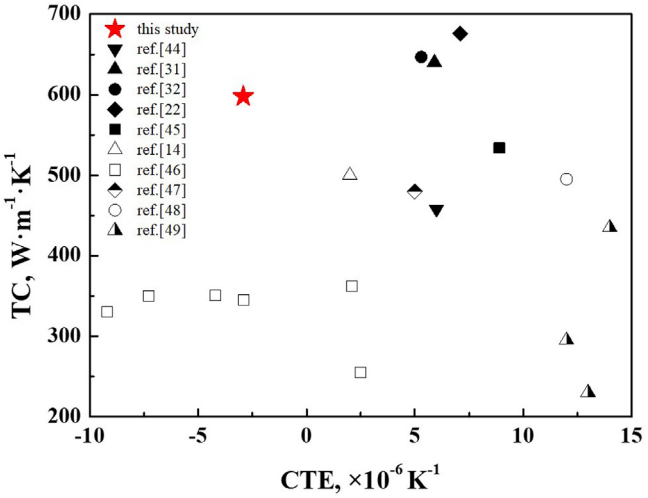

Fig. 12. Comparison of TC and CTE properties between the obtained 50GF/Cu–1Mo composite and published reported MMCs [14,22,31,32,46–51]. (A colour version of this figure can be viewed online.)

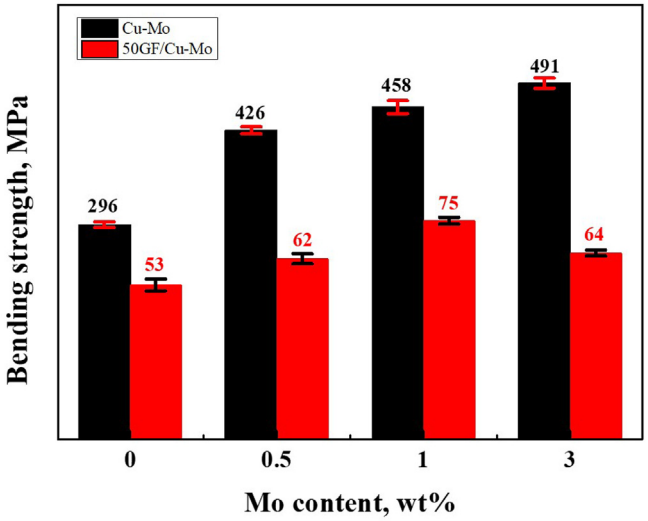

Fig. 13. Bending strength of the obtained 50GF/Cu composites and pure copper with different Mo content. (A colour version of this figure can be viewed online.)

interplanar crystal spacing of GFs. It could be speculated that the decrease of the lattice deformation caused by residual thermal stress counteracted the increase of the lattice constant caused by raising temperature, which led to the thermal expansion anomaly phenomenon in the Z direction. The residual stress disappeared with temperature, and the crystal lattice of Cu and GF still expanded, resulting in the increasing value of the Z-CTE of the composites. The introduction of Mo did not strengthen the left shift of the Cu and GF peaks in the GF/Cu–Mo composites, which suggested the stability of the residual stress value in the Cu matrix. Also, it is well-known that the internal stress produced by the mismatch in the thermal expansion between Cu and GF may lead to small cracks in the GF/Cu composite (difficult to observe), which may have a lagging effect on the CTE test of the composite.

Fig. 12 shows the comparison of thermal properties between our work and some previous studies. The obtained 50GF/Cu–1Mo composite in this study exhibited better comprehensive thermal performance. It is possible to obtain required performance by controlling the volume fraction and the orientation of reinforcement. The mechanical properties still needs to be improved by enhancing the matrix and the bond strength. It is believed that the GF/Cu composites are one of the potential advanced management materials, and have space for improvement.

3.4. Mechanical properties

Fig. 13 represented the bending strength of the 50GF/Cu composite with various Mo content. The Cu–Mo alloys are ductile materials and their bending strength was calculated according to the maximum bending force (when fracture occurred). It could be observed that the bending strength of the Cu–Mo alloy followed an increasing trend with Mo content. However, the bending

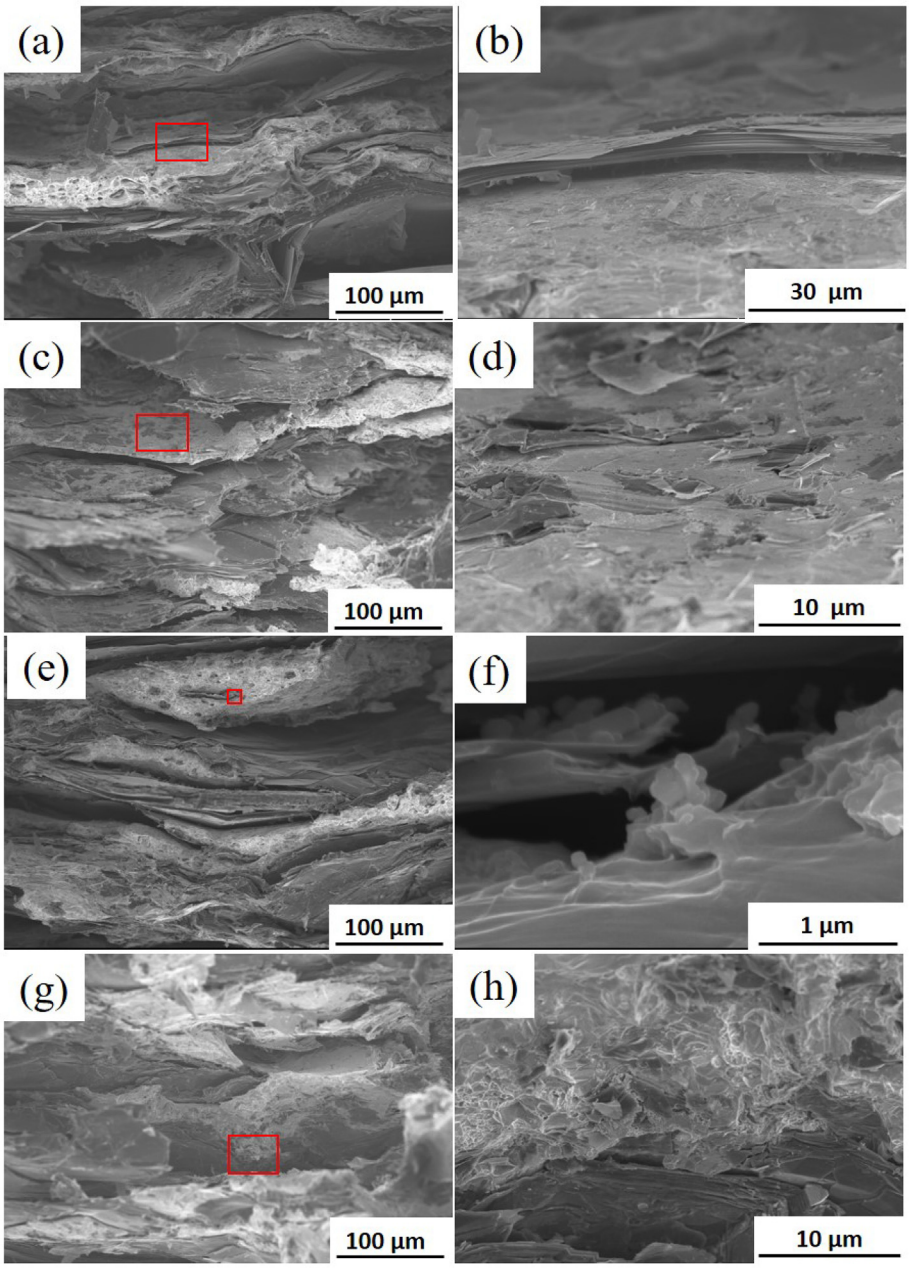

Fig. 14. SEM images of the fracture surface (a, c, e, g) and enlarged view (b, d, f, h) of Cu/50GF/Cu, 50GF/Cu-0.5Mo, 50GF/Cu–1Mo, 50GF/Cu–3Mo composites. (A colour version of this figure can be viewed online.)

strength of 50GF/Cu–Mo composites increased first and then decreased with higher Mo content. The bending strength of 50GF/Cu composite with 1 *wt%* Mo reached the highest value of 75 *MPa*, but fell to 64 *MPa* with 3 *wt%* Mo. Kang et al. [52] verified that particulate-reinforced metal matrix composites exhibited improved mechanical properties with increasing amount of nanometric particulates. However, the agglomeration of the high-volume fraction nanometric particles in the metal matrix gentled the strengthening effect on the mechanical properties. Fig. 6 shows submicron Mo particulates distributed in the Cu grain boundaries, pinning the boundaries and refining the Cu particles. The bending strength of the Cu–3Mo alloy (491 *MPa*) is about 65.9% higher than the pure Cu (296 *MPa*), which may be attributed to the Mo's refining effect on Cu particles. In addition, the Mo "rivet" at the Cu-GF interface in Fig. 8 combined Cu matrix with GFs. The enhanced Cu-GF interfacial bonding improved the bending strength of the 50GF/Cu–1Mo composite to 75 *MPa*. The aggregation of Mo particles near the GFs aggravated owing to higher content. Dramatically, the bending strength of the composite with 3 *wt%* Mo fell to 64 *MPa*, revealing the side effect of Mo aggregation. On the one hand, Figs. 6 and 7(d) had proven that the aggregation of Mo particles weakened their effect on grain refinement. The 50GF/Cu–3Mo composite had larger Cu grain size compared with its counterpart with 1 *wt%* Mo. On the other hand, the formation of Mo_2C also could be explained as the Mo erosion on the GFs. As a result, the variation of the bending strength of 50GF/Cu–Mo could be attributed to the dual function of Mo addition on the Cu-GF interface and the mechanical properties strengthening of the Cu matrix.

Fig. 14 displays the fracture surface of the 50GF/Cu composites with different Mo content. It can be observed that Cu and GF are stacked layer by layer, presenting obvious orientation. It should be noted that the fracture model of the 50GF/Cu–Mo composites exhibited brittle fracture. Dimples in the Cu matrix were examined, and the tearing in the GFs occurred. It can be indicated that the brittle fracture of the composites had great correlation with the GFs, which cannot be ignored. The enlarged views of the 50GF/Cu composites in Fig. 14(b) shows that the GFs separated from the Cu matrix without Mo after fracture of the composite, which meant the Cu-GF interfacial debonding started. With 0.5 *wt%* Mo, the Cu matrix could catch a small amount of GFs surface layers (shown in Fig. 14(d)). Fig. 14(f) displays the pinning effect of Mo particles on GFs and Cu. The GF was tightly wrapped in Cu when the fracture occurred with 3 *wt%* Mo (Fig. 14(h)), indicating strong bonding between Cu and GF. Thus, the introduction of Mo can enhance Cu-GF interfacial bonding, changing from the purely physical connection into the physical-chemical synergy.

4. Conclusions

The 50GF/Cu–Mo composites were fabricated by tape-casting with hot-pressing sintering. Tape-casting enhanced the alignment of GFs (2D flaky material) with small radial dimensions. The 50 *vol%* GF/Cu composites with 1 *wt%* Mo had high XY-TC of 598 $W \cdot m^{-1} \cdot K^{-1}$, low Z-CTE of $-2.92\times10^{-6}K^{-1}$ (25–100 °C), which was comparable to the thermal expansion of semiconductors. The introduction of Mo remarkably improved the overall performance of the GF/Cu composites. Mo_2C particles formed at high temperature contributed to lower CTE and enhanced bending strength of the composites. Furthermore, the TC of the Cu matrix and bulk composites deceased in virtue of the enhancement of the phonon dispersion through Mo particles in the Cu matrix and Cu-GF interface. Undeniably, the Cu–C interface modification and the alignment of 2D flaky materials had the decisive influence on the thermal and mechanical properties of the composite. The distribution, size and amount of particles in the matrix and at the interface should be further controlled for better performance.

Author contributions section

1. Qianyue Cui and Cunguan Chen conceived and designed the study, and wrote the paper.
2. Chengwei Yu and Tianxing Lu performed the experiments.
3. Haiming Long and Shuhao Yan processed raw data.
4. Junjie Hao and Alex A. Volinsky reviewed and edited the manuscript.
5. All authors read and approved the manuscript.

Declaration of competing interest

We declare that we have no financial and personal relationships with other people or organizations that can inappropriately influence our work. There is no professional or other personal interest of any nature or kind in any product, service and/or company that represents a conflict of interest in connection with the work submitted.

Acknowledgments

This work was supported by the Fundamental Research Funds for the Central Universities (Grant No. FRF-TP-18-029A2) and the State Key Lab of Advanced Metals and Materials (Grant No. 2019-Z10).

References

[1] A. Moore, L. Shi, Emerging challenges and materials for thermal management of electronics, Mater. Today 17 (2014) 163–174, https://doi.org/10.1016/j.mattod.2014.04.003.
[2] K. Mizuuchi, K. Inoue, Y. Agari, Trend of the development of metal-based heat dissipative materials, Microelectron. Reliab. 79 (2017) 5–19, https://doi.org/10.1016/j.microrel.2017.10.007.
[3] S.S. Sidhu, S. Kumar, A. Batish, Metal matrix composites for thermal management: a review, Crit. Rev. Solid State Mater. Sci. 41 (2) (2016) 132–157, https://doi.org/10.1080/10408436.2015.1076717.
[4] L. Wang, J. Li, G. Bai, N. Li, X. Wang, H. Zhang, J. Wang, M.J. Kim, Interfacial structure evolution and thermal conductivity of Cu-Zr/diamond composites prepared by gas pressure infiltration, J. Alloys Compd. 781 (2019) 800–809, https://doi.org/10.1016/j.jallcom.2018.12.053.
[5] C. Li, X. Wang, L. Wang, J. Li, H. Li, H. Zhang, Interfacial characteristic and thermal conductivity of Al/diamond composites produced by gas pressure infiltration in a nitrogen atmosphere, Mater. Des. 92 (2016) 643–648, https://doi.org/10.1016/j.matdes.2015.12.098.
[6] Y. Huang, Y. Su, S. Li, Q. Ouyang, G. Zhang, L. Zhang, D. Zhang, Fabrication of graphite film/aluminum composites by vacuum hot pressing: process optimization and thermal conductivity, Compos. B Eng. 107 (2016) 43–50, https://doi.org/10.1016/j.compositesb.2016.09.051.
[7] A.M. Abyzov, S.V. Kidalov, F.M. Shakhov, High thermal conductivity composite of diamond particles with tungsten coating in a copper matrix for heat sink application, Appl. Therm. Eng. 48 (2012) 72–80, https://doi.org/10.1016/j.applthermaleng.2012.04.063.
[8] Y. Zhang, H. Zhang, J. Wu, X. Wang, Enhanced thermal conductivity in copper matrix composites reinforced with titanium-coated diamond particles, Scripta Mater. 65 (12) (2011) 1097–1100, https://doi.org/10.1016/j.scriptamat.2011.09.028.
[9] A.A. Balandin, Thermal properties of graphene and nanostructured carbon materials, Nat. Mater. 10 (2011) 569–581, https://doi.org/10.1038/nmat3064.
[10] P. Kim, L. Shi, A. Majumdar, P.L. McEuen, Thermal transport measurements of individual multiwalled nanotubes, Phys. Rev. Lett. 87 (2001) 215502, https://doi.org/10.1103/PhysRevLett.87.215502.
[11] P. Eric, M. David, W. Qian, G. Kenneth, D. Hongjie, Thermal conductance of an individual single-wall carbon nanotube above room temperature, Nano Lett. 6 (1) (2006) 96–100.
[12] M. Inagaki, Y. Kaburagi, Y. Hishiyama, Thermal management material: Graphite, Adv. Eng. Mater. 16 (5) (2014) 494–506, https://doi.org/10.1002/adem.201300418.
[13] A. Boden, B. Boerner, P. Kusch, I. Firkowska, S. Reich, Nanoplatelet size to control the alignment and thermal conductivity in copper-graphite composites, Nano Lett. 14 (6) (2014) 3640–3644, https://doi.org/10.1021/nl501411g.
[14] I. Firkowska, A. Boden, B. Boerner, S. Reich, The origin of high thermal

conductivity and ultralow thermal expansion in copper-graphite composites, Nano Lett. 15 (7) (2015) 4745–4751, https://doi.org/10.1021/acs.nanolett.5b01664.
[15] M. Cao, D. Xiong, Z. Tan, G. Ji, B. Amin-Ahmadi, Q. Guo, G. Fan, C. Guo, Z. Li, D. Zhang, Aligning graphene in bulk copper: nacre-inspired nanolaminated architecture coupled with in-situ processing for enhanced mechanical properties and high electrical conductivity, Carbon 117 (2017) 65–74, https://doi.org/10.1016/j.carbon.2017.02.089.
[16] C. Zhou, W. Huang, Z. Chen, G. Ji, M. Wang, D. Chen, H. Wang, In-plane thermal enhancement behaviors of Al matrix composites with oriented graphite flake alignment, Compos. B Eng. 70 (2015) 256–262, https://doi.org/10.1016/j.compositesb.2014.11.018.
[17] K. Chu, X. Wang, F. Wang, Y. Li, D. Huang, H. Li, W. Ma, F. Liu, H. Zhang, Largely enhanced thermal conductivity of graphene/copper composites with highly aligned graphene network, Carbon 127 (2017) 102–112, https://doi.org/10.1016/j.carbon.2017.10.099.
[18] J. Lloyd, E. Neubauer, J. Barcena, W. Clegg, Effect of titanium on copper-titanium/carbon nanofibre composite materials, Compos. Sci. Technol. 70 (16) (2010) 2284–2289, https://doi.org/10.1016/j.compscitech.2010.05.002.
[19] S. Dorfman, D. Fuks, M. Suery, Diffusivity of carbon in copper- and silver-based composites, J. Mater. Sci. 34 (1) (1999) 77–81, https://doi.org/10.1023/A:1004461423717.
[20] D.A. Mortimer, M. Nicholas, The wetting of carbon by copper and copper alloys, J. Mater. Sci. 5 (2) (1970) 149–155, https://doi.org/10.1007/BF00554633.
[21] Y.Z. Zhan, G. Ren Guo, H.G. Xi, X.F. Zhen, H. Chen, Y. Chen, Microstructures and properties of graphene-Cu/Al composite prepared by a novel process through clad forming and improving wettability with copper, Adv. Eng. Mater. 17 (2015) 663–668, https://doi.org/10.1002/adem.201400173.
[22] H. Bai, C. Xue, J. Lyu, J. Li, C. Guoxin, J. Yu, C. Lin, D. Lv, L. Xiong, Thermal conductivity and mechanical properties of flake graphite/copper composite with a boron carbide-boron nano-layer on graphite surface, Composites Part A Applied Science and Manufacturing 106 (2017) 42–51, https://doi.org/10.1016/j.compositesa.2017.11.019.
[23] Y. Zhu, H. Bai, C. Xue, R. Zhou, Q. Xu, P. Tao, C. Wang, J. Wang, N. Jiang, Thermal conductivity and mechanical properties of a flake graphite/Cu composite with a silicon nano-layer on a graphite surface, RSC Adv. 6 (2016) 98190–98196, https://doi.org/10.1039/C6RA17804A.
[24] K. Chu, F. Wang, Y. biao Li, X. hu Wang, D. jian Huang, Z. rong Geng, Interface and mechanical/thermal properties of graphene/copper composite with Mo_2C nanoparticles grown on graphene, Compos. Appl. Sci. Manuf. 109 (2018) 267–279, https://doi.org/10.1016/j.compositesa.2018.03.014.
[25] S. Ma, N. Zhao, C. Shi, E. Liu, C. He, F. He, L. Ma, Mo_2C coating on diamond: different effects on thermal conductivity of diamond/Al and diamond/Cu composites, Appl. Surf. Sci. 402 (2017) 372–383, https://doi.org/10.1016/j.apsusc.2017.01.078.
[26] L. Wang, J. Li, Z. Che, X. Wang, H. Zhang, J. Wang, M.J. Kim, Combining Cr precoating and Cr alloying to improve the thermal conductivity of diamond particles reinforced Cu matrix composites, J. Alloys Compd. 749 (2018) 1098–1105, https://doi.org/10.1016/j.jallcom.2018.03.241.
[27] K. Chu, Z. Liu, C. Jia, H. Chen, X. Liang, W. Gao, W. Tian, H. Guo, Thermal conductivity of SPS consolidated Cu/diamond composites with Cr-coated diamond particles, J. Alloys Compd. 490 (1) (2010) 453–458, https://doi.org/10.1016/j.jallcom.2009.10.040.
[28] Q. Kang, X. He, S. Ren, L. Zhang, M. Wu, C. Guo, W. Cui, X. Qu, Preparation of copper-diamond composites with chromium carbide coatings on diamond particles for heat sink applications, Appl. Therm. Eng. 60 (1) (2013) 423–429, https://doi.org/10.1016/j.applthermaleng.2013.05.038.
[29] J. Li, H. Zhang, L. Wang, Z. Che, Y. Zhang, J. Wang, M.J. Kim, X. Wang, Optimized thermal properties in diamond particles reinforced copper-titanium matrix composites produced by gas pressure infiltration, Compos. Appl. Sci. Manuf. 91 (2016) 189–194, https://doi.org/10.1016/j.compositesa.2016.10.005.
[30] S. Ren, J. Chen, X. He, X. Qu, Effect of matrix-alloying-element chromium on the microstructure and properties of graphite flakes/copper composites fabricated by hot pressing sintering, Carbon 127 (2018) 412–423, https://doi.org/10.1016/j.carbon.2017.11.033.
[31] R. Zhang, X. He, H. Chen, X. Qu, Effect of alloying element Zr on the microstructure and properties of graphite flake/Cu composites fabricated by vacuum hot pressing, J. Alloys Compd. 770 (2019) 267–275, https://doi.org/10.1016/j.jallcom.2018.08.107.
[32] G. Bai, N. Li, X. Wang, J. Wang, M.J. Kim, H. Zhang, High thermal conductivity of Cu-B/diamond composites prepared by gas pressure infiltration, J. Alloys Compd. 735 (2018) 1648–1653, https://doi.org/10.1016/j.jallcom.2017.11.273.
[33] Q. Che, X. Chen, Y. Ji, Y. Li, L. Wang, S. Cao, Y. Jiang, Z. Wang, The influence of minor titanium addition on thermal properties of diamond/copper composites via in situ reactive sintering, Mater. Sci. Semicond. Process. 30 (2015) 104–111, https://doi.org/10.1016/j.mssp.2014.09.050.
[34] X. Liang, C. Jia, K. Chu, H. Chen, Predicted interfacial thermal conductance and thermal conductivity of diamond/Al composites with various interfacial coatings, Rare Met. 30 (5) (2011) 544–549, https://doi.org/10.1007/s12598-011-0427-x.
[35] J. Chen, S. Ren, X. He, X. Qu, Properties and microstructure of nickel-coated graphite flakes/copper composites fabricated by spark plasma sintering, Carbon 121 (2017) 25–34, https://doi.org/10.1016/j.carbon.2017.05.082.
[36] B. Wang, G. Wang, H. Wang, Hybrids of Mo_2C nanoparticles anchored on graphene sheets as anode materials for high performance lithium-ion batteries, J. Mater. Chem. 3 (2015) 17403–17411, https://doi.org/10.1039/C5TA03929K.
[37] Q. Gao, X. Zhao, Y. Xiao, D. Zhao, M. Cao, A mild route to mesoporous Mo_2C-C hybrid nanospheres for high performance lithium-ion batteries, Nanoscale 6 (2014) 6151–6157, https://doi.org/10.1039/C3NR06678A.
[38] K.F. Wang, G.D. Sun, Y.D. Wu, G.H. Zhang, Fabrication of ultrafine and high-purity tungsten carbide powders via a carbothermic reduction-carburization process, J. Alloys Compd. 784 (2019) 362–369, https://doi.org/10.1016/j.jallcom.2019.01.055.
[39] C.W. Nan, R. Birringer, D.R. Clarke, H. Gleiter, Effective thermal conductivity of particulate composites with interfacial thermal resistance, J. Appl. Phys. 81 (10) (1997) 6692–6699, https://doi.org/10.1063/1.365209.
[40] C.W. Nan, G. Liu, Y. Lin, M. Li, Interface effect on thermal conductivity of carbon nanotube composites, Appl. Phys. Lett. 85 (16) (2004) 3549–3551, https://doi.org/10.1063/1.1808874.
[41] M. Murakami, N. Nishiki, K. Nakamura, J. Ehara, H. Okada, T. Kouzaki, K. Watanabe, T. Hoshi, S. Yoshimura, High-quality and highly oriented graphite block from polycondensation polymer films, Carbon 30 (2) (1992) 255–262, https://doi.org/10.1016/0008-6223(92)90088-E.
[42] E.H. Kerner, The elastic and thermo-elastic properties of composite media, Proc. Phys. Soc. B 69 (8) (1956) 808–813, https://doi.org/10.1088/0370-1301/69/8/305.
[43] P. Turner, Thermal-expansion stress in reinforced plastics, J. Res. Natl. Bur. Stand. 37 (1946) 250–339, https://doi.org/10.6028/jres.037.015.
[44] J. Kováčik, E. Š, Thermal expansion of Cu/graphite composites: effect of copper coating, Kovove Mater. 49 (2011) 411, https://doi.org/10.4149/km_2011_6_411.
[45] H. Kurita, T. Miyazaki, A. Kawasaki, Y. Lu, J.-F. Silvain, Interfacial microstructure of graphite flake reinforced aluminum matrix composites fabricated via hot pressing, Compos. Appl. Sci. Manuf. 73 (2015) 125–131, https://doi.org/10.1016/j.compositesa.2015.03.013.
[46] K. Chu, X. hu Wang, Y. biao Li, D. jian Huang, Z. rong Geng, X. long Zhao, H. Liu, H. Zhang, Thermal properties of graphene/metal composites with aligned graphene, Mater. Des. 140 (2018) 85–94, https://doi.org/10.1016/j.matdes.2017.11.048.
[47] C.Y. Guo, X.B. He, S.B. Ren, X.H. Qu, Thermal properties of diamond/Al composites by pressure infiltration: comparison between methods of coating Ti onto diamond surfaces and adding Si into Al matrix, Rare Met. 35 (3) (2016) 249–255, https://doi.org/10.1007/s12598-015-0672-5.
[48] V. Oddone, B. Boerner, S. Reich, Composites of aluminum alloy and magnesium alloy with graphite showing low thermal expansion and high specific thermal conductivity, Sci. Technol. Adv. Mater. 18 (1) (2017) 180–186, https://doi.org/10.1080/14686996.2017.1286222.
[49] S. Park, D. Kim, R. Lee, I. Son, Thermal conductivity and microstructure of copper coated graphite composite by spark plasma sintering process, Arch. Metall. Mater. 62 (2) (2017) 1303–1306, https://doi.org/10.1515/amm-2017-0197.
[50] V. Oddone, J. Segl, M. Prakasam, M.T. Hartmann, J.-F. Silvain, C. Edtmaier, S. Reich, Isotropic thermal expansion in anisotropic thermal management composites filled with carbon fibres and graphite, J. Mater. Sci. 53 (15) (2018) 10910–10919, https://doi.org/10.1007/s10853-018-2373-6.
[51] A. Shin, Y.I. Kim, S.H. Ko, J.H. Han, Study on microstructure and thermal properties of a CNF/Cu nanocomposite fabricated using chemical mixing, J. Alloys Compd. 737 (2018) 21–30, https://doi.org/10.1016/j.jallcom.2017.12.034.
[52] Y.C. Kang, S.L.I. Chan, Tensile properties of nanometric Al2O3 particulate-reinforced aluminum matrix composites, Mater. Chem. Phys. 85 (2) (2004) 438–443, https://doi.org/10.1016/j.matchemphys.2004.02.002.